

# Studies on high-pressure phase transitions and melt structure of PbO<sub>2</sub>: An analog for silica

Bora Kalkan,<sup>\*1,2</sup> B. K. Godwal,<sup>3</sup> Jinyuan Yan,<sup>2</sup> and Raymond Jeanloz<sup>3,4</sup>

<sup>1</sup>*Earth and Planetary Sciences Department, University of California, Santa Cruz, CA, 95064, USA*

<sup>2</sup>*Advanced Light Source, Lawrence Berkeley National Laboratory, Berkeley, CA, 94720, USA*

<sup>3</sup>*Department Earth and Planetary Science, University of California, Berkeley, CA, USA*

<sup>4</sup>*Department Astronomy and Miller Institute for Basic Research in Science, University of California, Berkeley, CA, USA*

## Abstract

In situ x-ray diffraction measurements and inverse Monte Carlo simulations of pair distribution functions were used to study the structural response of PbO<sub>2</sub> under pressure, and to characterize the local structure of liquid-PbO<sub>2</sub>. Two phase transitions are observed upon room-temperature compression of crystalline PbO<sub>2</sub> up to ~65 GPa. The starting mixture of rutile structured  $\beta$ -PbO<sub>2</sub> and orthorhombic  $\alpha$ -PbO<sub>2</sub> undergoes a transition to a ZrO<sub>2</sub>-type orthorhombic phase with space group *Pbca* at ~21 GPa. Above 42 GPa, the *Pbca* phase transforms to a cotunnite-type phase with space group *Pnam*. This study also reports short-range order in liquid-PbO<sub>2</sub> showing ~8-9-fold and 4-5-fold coordination around Pb and O atoms, respectively.

## I. INTRODUCTION

Silica ( $\text{SiO}_2$ ) is a major constituent of planetary interiors. At ambient pressure, crystalline silica includes the quartz and its polymorphs: cristobalite and tridymite [1]. Thereafter,  $\alpha$ -quartz shows a series of structural phase transitions with increasing pressure: quartz  $\rightarrow$  coesite  $\rightarrow$  stishovite  $\rightarrow$   $\text{CaCl}_2$ -type  $\rightarrow$   $\alpha$ - $\text{PbO}_2$   $\rightarrow$  pyrite-type (268 GPa, 1800 K) [2-4]. Post pyrite-type structures are identified using first-principles calculations [5-8]. At low temperatures, the transition from pyrite- to  $\text{Fe}_2\text{P}$ -type is expected to occur at  $\sim 750$  GPa. Above 1000 K, silica first transforms from the pyrite-type structure to cotunnite, and then to  $\text{Fe}_2\text{P}$ -type [9]. Lyle et al [10] recently predicted silica to transform from the 9-coordinated  $\text{Fe}_2\text{P}$  polymorph to a 10-coordinated orthorhombic tetragonal structure ( $I_4/mmm$ ) with concomitant metallization near 10 TPa.

Analogous to  $\text{SiO}_2$  such as  $\text{TiO}_2$ ,  $\text{GeO}_2$  and  $\text{SnO}_2$  have been studied extensively, the interest being to experimentally document the high-pressure phases of  $\text{SiO}_2$  at relatively low pressures. At ambient conditions, rutile is the most stable phase of  $\text{TiO}_2$ , and it undergoes a sequence of phase transitions with pressure: rutile  $\rightarrow$   $\alpha$ - $\text{PbO}_2$ -type  $\rightarrow$  orthorhombic-I  $\rightarrow$  orthorhombic-II (related to pyrite-type)  $\rightarrow$  cotunnite-type (above 50 GPa)  $\rightarrow$   $\text{Fe}_2\text{P}$  type (210 GPa, 4000 K) [11-13]. It is also predicted to transform from the  $\text{Fe}_2\text{P}$ -type to orthorhombic the tetragonal phase ( $I_4/mmm$ ) near 6.5 Mbar [10,14].  $\text{GeO}_2$  occurs in  $\alpha$ -quartz and rutile structures at ambient conditions, with several high-pressure transitions:  $\alpha$ -quartz  $\rightarrow$   $\text{P}2_1/c$   $\rightarrow$  rutile  $\rightarrow$   $\text{CaCl}_2$   $\rightarrow$   $\alpha$ - $\text{PbO}_2$   $\rightarrow$  pyrite-type [2,15-17]. Ab-initio calculations predict the sequence: rutile  $\rightarrow$   $\text{CaCl}_2$   $\rightarrow$   $\alpha$ - $\text{PbO}_2$   $\rightarrow$  pyrite-type  $\rightarrow$  cotunnite (300 GPa)  $\rightarrow$   $\text{Fe}_2\text{P}$  (600 GPa) [13,18]. Haines and Leger [19] studied  $\text{SnO}_2$  up to 49 GPa using non-hydrostatic pressure media (grease and 16:3:1 methanol-ethanol-water mixtures), observing the structural transitions rutile  $\rightarrow$   $\text{CaCl}_2$   $\rightarrow$   $\alpha$ - $\text{PbO}_2$   $\rightarrow$  pyrite-type. This is similar to the high-pressure sequence found for  $\text{GeO}_2$ , the difference lying in the transition pressures. For example,

the pyrite phase of GeO<sub>2</sub> occurs in the range 70-90 GPa [2, 20], compared to SnO<sub>2</sub> for which it is observed around 49 GPa. Using x-ray diffraction at high pressures and temperatures with argon as pressure medium, Shieh et al. [21] observed a rutile → CaCl<sub>2</sub> → pyrite → ZrO<sub>2</sub> → cotunnite structural sequence in SnO<sub>2</sub>. The ZrO<sub>2</sub> (Pbca) phase is found between 50 and 74 GPa under room-temperature compression, and the cotunnite phase observed at 54-117 GPa when laser heated between 1200 -1500 K and then quenched.

Lead oxide (PbO<sub>2</sub>) is another promising analog for SiO<sub>2</sub>. Two forms of lead oxide are found as minerals on Earth's surface, orthorhombic  $\alpha$ -PbO<sub>2</sub> (scrutinyite) and tetragonal rutile structured  $\beta$ -PbO<sub>2</sub> (plattnerite) [4]. Using x-ray diffraction with a non-hydrostatic pressure medium (grease), Haines et al. observed the sequence of transitions in  $\beta$ -PbO<sub>2</sub>: rutile → (4GPa) CaCl<sub>2</sub> → (7GPa)Pa-3 → (11.4GPa) Pbca → (> 29GPa) cotunnite [16, 19]. The  $\alpha$ -PbO<sub>2</sub> form also adopted the pyrite phase at 7 GPa, and showed the coexistence of *Pbca* and *Pnam* phases from 29 to 47 GPa. Grocholski et al. [4] studied PbO<sub>2</sub> polymorphs up to 140 GPa in a laser-heated diamond-anvil cell under more hydrostatic conditions, with argon as a pressure medium. They applied laser heating to avoid the multiphase mixtures formed in Haines et al.'s experiments at room temperature [19]. Further, they observed the baddeleyite-type structure in room-temperature compression measurements, which was absent from Haines et al.'s results [19]. It is also to be noted that in PbO<sub>2</sub> the cotunnite phase is observed at low pressures (24 GPa) using laser heating [4], as compared to SnO<sub>2</sub> for which it occurs at 54 GPa [19], suggesting that PbO<sub>2</sub> is the better analog for silica. The baddeleyite phase that was observed by Grocholski et al. [4] in the 30-40 GPa range was absent from Haines et al.'s data [19]. Grocholski et al.'s [4], laser heating of  $\beta$ -PbO<sub>2</sub> succeeded in preventing the mixed-phase region (Pbca (OI) and Cotunnite (Pnam) from 29-47 GPa) in Haines et al.'s studies [19], and documented a pure cotunnite phase. The main difference between their

studies was the degree of hydrostaticity deviatoric stress and strain achieved through laser heating and use of different pressure media. We carried out our study with neon as a pressure medium to check the sensitivity of the phase-transition pressures on hydrostaticity deviatoric stress and strain.

In addition, we carried out high-pressure X-ray diffraction measurements to study the structure of liquid  $\text{PbO}_2$ , the closest analogue to liquid  $\text{SiO}_2$  at ultrahigh pressures, as compared with  $\text{SnO}_2$ ,  $\text{GeO}_2$  and  $\text{TiO}_2$ : liquid  $\text{PbO}_2$  is expected to become metallic at low pressures. At ambient conditions,  $\text{PbO}_2$  melts at 365 K, compared to other analogues, which melt at high temperatures and show similar structural changes at low pressures as (non-metallic) silica. Thus, studies on melt structure at moderate pressures can be important for understanding metallic silica at extreme conditions. The melting temperature and melt-structure properties of analog materials more generally provide important insights into silica phases at extreme pressure-temperature conditions [22]. The laboratory data in fact provide benchmarks for first-principles density functional based molecular dynamic simulations representing the current means of exploring the properties of giant planetary interiors [23]. These high-pressure results on fluids are of interest because melting is the main process by which the interiors of terrestrial planets evolve, and melting phenomena and melt structure are of widespread importance in physical sciences.

## II. METHODS

Polycrystalline  $\text{PbO}_2$  (Sigma Aldrich > 99% purity) was ground to micron-sized grains and loaded into a symmetric diamond cell and a BX-90 diamond-anvil cell equipped with tungsten resistive heater; these are driven by a gas membrane for the room temperature-high pressure and high temperature-high pressure experiments, respectively. Type Ia diamonds with 200  $\mu\text{m}$ -diameter culets were mounted on tungsten carbide seats on the upstream side of each cell. We used

BN backing plates with opening angles on the detector side that allowed diffraction data to be collected up to maximum scattering vector-magnitude  $Q = 7 \text{ \AA}^{-1}$ , corresponding to a resolution in radial distribution functions  $\Delta r \sim 0.89 (\pm 0.04) \text{ \AA}$ . Sample chambers were formed by drilling holes with a diameter of  $80 \text{ }\mu\text{m}$  in Re foil that was pre-indented to  $30 \text{ }\mu\text{m}$  thickness. Liquefied neon served as the pressure-transmitting medium in compression experiments. Ruby spheres of  $\leq 5 \text{ }\mu\text{m}$  diameter were placed inside the sample chamber, and the ruby fluorescence technique was used to determine the pressure [24]. On-line ruby ( $\text{Al}_2\text{O}_3:\text{Cr}^{3+}$ ) fluorescence was used to determine pressure of the hot sample. Temperature was measured to an accuracy of  $\pm 5 \text{ K}$  up to  $900 \text{ K}$  using a K-type thermocouple next to the diamond culet [25].

Angle dispersive X-ray diffraction experiments were performed at beamline 12.2.2 at the Lawrence Berkeley National Laboratory Advanced Light Source [26]. A monochromatic X-ray beam with  $\lambda = 0.4959 \text{ \AA}$  ( $25.00 \text{ keV}$ ) was focused to an approximate size of  $10 \text{ }\mu\text{m} \times 10 \text{ }\mu\text{m}$ . Diffracted X rays were collected by a Mar345 detector at a distance of  $(331.4 \pm 0.1) \text{ mm}$ . Detector distance and orientation were calibrated using a  $\text{LaB}_6$  standard. The diffraction images were radially integrated using the programs FIT2D [27] and DIOPTAS [28]. The Celref program [29] was used to refine unit cell parameters. To determine the structural parameters, the diffraction patterns were analyzed by performing Rietveld refinements using the GSAS software [30].

For room temperature-high pressure experiments, the sample was pressurized upon compression with 1-3 GPa and 3-6 GPa steps in the pressure ranges of  $P < 32 \text{ GPa}$  and  $P > 32 \text{ GPa}$ , respectively. In the case of high temperature-high pressure measurements, the sample was taken to the desired pressure first, and then put through a heating and cooling cycle. We observed consistent pressure shifts during each cycle, caused by thermal expansion of the diamond-cell components; these were compensated with gas driven pressure. Complete melting of  $\text{PbO}_2$  is

identified by loss of long-range order, indicated by the disappearance of x-ray diffraction peaks of the crystalline phase and a simultaneous increase in diffuse scattering over the entire  $2\theta$  range.

The technique used to obtain partial structure factors and to derive structural models of liquid-PbO<sub>2</sub> was the empirical potential structure refinement method, EPSR [31]. A Monte Carlo computer simulation of the system PbO<sub>2</sub> was created using 1000 Pb and 2000 O atoms within a cubic box. Atoms interacted via a Lennard-Jones (12-6) potential and Coulomb term [32]. The parameters defining the interatomic pair potentials used in the structure refinements, taken from Ref. [33] and [34], are as follows for O and Pb:  $\epsilon_O = 0.1625 \text{ kJ mol}^{-1}$ ,  $\sigma_O = 3.6 \text{ \AA}$ ,  $q_O = -2e$ , and  $\epsilon_{Pb} = 0.20 \text{ kJ mol}^{-1}$ ,  $\sigma_{Pb} = 2.40 \text{ \AA}$ ,  $q_{Pb} = 4e$ . The edge lengths of the simulation cubic box with periodic boundary conditions for liquid-PbO<sub>2</sub> are  $37.11 \text{ \AA}$  and  $36.84 \text{ \AA}$ , derived from the atomic number densities of  $0.0587 \text{ atoms/\AA}^3$  (at 901 K/4 GPa) and  $0.0600 \text{ atoms/\AA}^3$  (at 773 K/8 GPa) [35]. In addition, minimum distances of approach were set at:  $1.24 \text{ \AA}$  (Pb-Pb),  $1.73 \text{ \AA}$  (Pb-O) and  $2.21 \text{ \AA}$  (O-O) [32, 33]. A starting model was obtained by successive iterations (convergence in  $\sim 1200$  iterations) of the system under the reference potential at 901 K and 773 K. Structural parameters and their distributions reported here were obtained over many configurations ( $>15000$  iterations) of the models as they fluctuate about the final equilibrium energy, at which the structure factors of the model and experiment are in good agreement.

### III. RESULTS AND DISCUSSIONS

X-ray diffraction results shown in [Figure 1](#) confirm that the starting material was ~~dominantly~~ rutile structured  $\beta$ -PbO<sub>2</sub> ( $P4_2/mnm$ ,  $Z = 2$ ) with a small contribution of naturally occurring orthorhombic  $\alpha$ -PbO<sub>2</sub> ( $Pbcn$ ,  $Z = 4$ ). Rietveld refinement of the structure yielded lattice parameters  $a = b = 4.9342(2) \text{ \AA}$ ,  $c = 3.3736(2) \text{ \AA}$  and  $a = 4.9850(9) \text{ \AA}$ ,  $b = 5.8946(9) \text{ \AA}$ ,  $c =$

5.4538(8) Å for  $\beta$ -PbO<sub>2</sub> and  $\alpha$ -PbO<sub>2</sub>, respectively. The starting values for Pb and O atomic coordinates for the observed phases are listed in [Table 1](#).

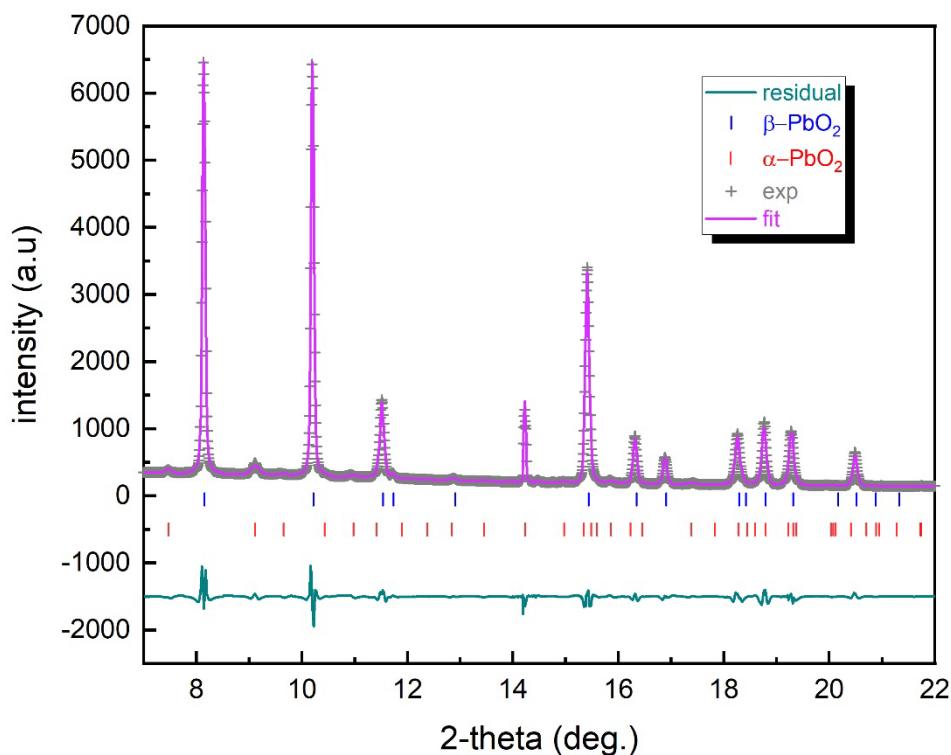


**Figure 1.** X-ray diffraction pattern of PbO<sub>2</sub> at ambient conditions, and the corresponding multi-phase Rietveld refinement. The plus symbols and red lines are observed and calculated patterns, respectively, and vertical bars denote allowed Bragg reflections for PbO<sub>2</sub> polymorphs. The bottom trace (green line) shows the difference between the observed and calculated patterns.

**Table 1.** Wyckoff positions of the phases of PbO<sub>2</sub>

Phase	Space group	Mineral name- Structure type	Z	Atomic parameters
1	<i>P4<sub>2</sub>/mnm</i>	$\beta$ -PbO <sub>2</sub> , rutile type, plattnerite	2	Pb 2a (0,0,0) O 4f (0.3066, 0.3066, 0)
2	<i>Pbcn</i>	$\alpha$ -PbO <sub>2</sub> , scrutinyite	4	Pb 4c (0, 0.1779, 0.250) O 8d (0.2685, 0.4010, 0.4248)
3	<i>Pbca</i>	ZrO <sub>2</sub> -type	8	Pb 8c (0.8861, 0.02504, 0.2638) O 8c (0.7963, 0.3800, 0.1381) O 8c (0.9777, 0.7500, 0.4901)
4	<i>Pnam</i>	Cotunnite-type	4	Pb 4c (0.260, 0.100, 0.250) O 4c (0.360, 0.430, 0.250) O 4c (0.020, 0.340, 0.750)

a. Compression at room temperature

Figure 2a shows the room temperature X-ray diffraction patterns for PbO<sub>2</sub> collected upon compression in the pressure range of 1.3-60 GPa. At pressures around 13.6 GPa, the intensities of the diffraction peaks for the β-PbO<sub>2</sub> and α-PbO<sub>2</sub> phases start to decrease, and these phases almost completely disappear at ~ 24.5 GPa. Bragg peaks for a new crystalline phase start to grow at 15.8 GPa, but β-PbO<sub>2</sub> and α-PbO<sub>2</sub> phases remain present. The new crystalline phase can be indexed as orthorhombic (space group *Pbca*, No. 61) with unit cell dimensions  $a = 10.2011(96)$  Å,  $b = 5.2540(52)$  Å,  $c = 5.1450(63)$  Å at 24.5 GPa, and it remains stable up to 39.3 GPa. The most intense peak of the orthorhombic phase (at around  $9.8^\circ 2\theta$ ) starts to disappear at 43.3 GPa, and new peaks appear. The diffraction pattern of this high-pressure phase can be indexed to the cotunnite-type orthorhombic structure (space group *Pnam*), which is also found to be stable at the highest pressure 62 GPa reached in the present study. Decompression from the ZrO<sub>2</sub>-type *Pbca* phase produces a pure α-PbO<sub>2</sub> (*Pbcn*) scrutinyite phase, with no evidence of any material reverting back to the starting phase, β-PbO<sub>2</sub> rutile structure (Figure 2b). These results are generally in good agreement with previous findings (Grocholski et al. [4]), and document common behavior for all group IV oxides that are compressed to phases with greater density than the rutile-type structure.

Examples of diffraction patterns from *Pbca* and *Pnam* orthorhombic phases obtained on compression to 34.3 GPa and 58 GPa, respectively, are depicted in Figure 3. The corresponding volume changes from 2.5 GPa to 34.3 GPa and to 58 GPa are in turn 19.7(4) % and 30.3(3) %, with cell constants obtained from structure refinements:  $a = b = 4.9327(7)$  Å,  $c = 3.3743(8)$  Å and  $a = 4.9583(18)$  Å,  $b = 5.8945(31)$  Å,  $c = 5.4692(28)$  Å for β-PbO<sub>2</sub> and α-PbO<sub>2</sub>, respectively. At 34.3 GPa, the refined cell constants are  $a = 10.1205(37)$  Å,  $b = 5.2253(8)$  Å,  $c = 4.9848(15)$  Å for the *Pbca* orthorhombic structure. The axial ratios  $a/c$  and  $b/c$  of the cotunnite structure are

1.6258(8) and 1.9403(9) at 58 GPa. These results show good agreement with those of cotunnite-type  $\text{ZrO}_2$  and  $\text{HfO}_2$ :  $a/c$ ,  $b/c$  = 1.678, 1.945 and 1.676, 1.951, respectively [36].

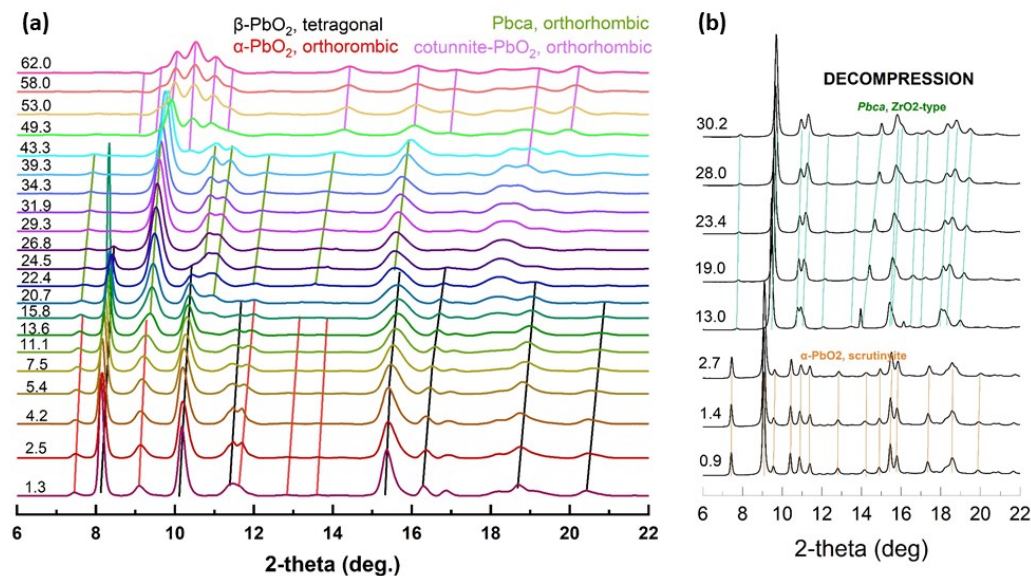


**Figure 2.** X-ray diffraction patterns collected at room temperature during compression (a) and decompression (b) of  $\text{PbO}_2$ . Solid lines follow the peak positions of relevant phases. Pressure values are listed to the left of each pattern.

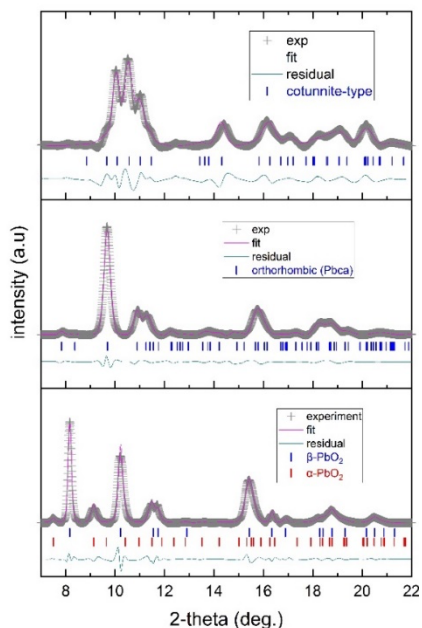


**Figure 3.** Room temperature X-ray diffraction patterns (*crosses*) collected at 2.5 GPa (bottom), 34.3 GPa (medium) and 58 GPa (top), and corresponding Rietveld refinement (*red curve*).

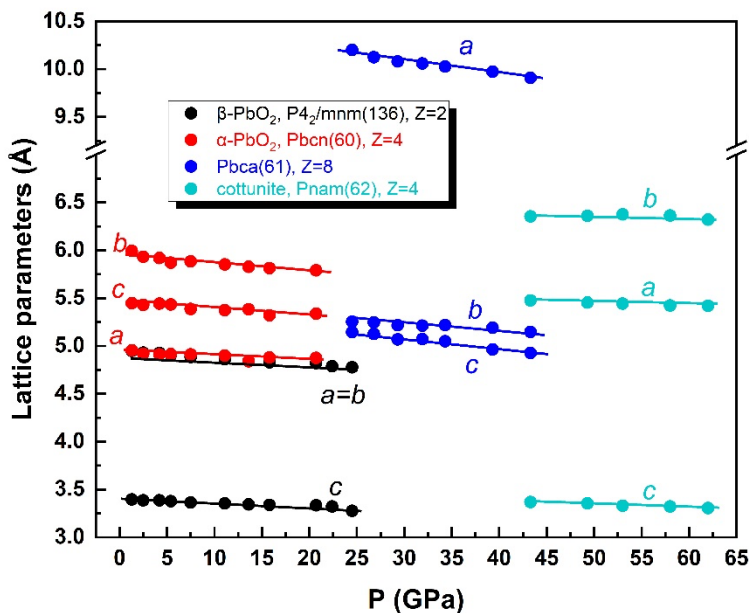


**Figure 4.** Lattice parameters measured on compression at room temperature. Solid lines are least squares fits.

At 24.5 GPa, the refined cell constants are  $a = 10.2011(49)$  Å,  $b = 5.2540(15)$  Å,  $c = 5.1450(16)$  Å for the orthorhombic phase with space group  $Pbca$ , which are comparable to  $ZrO_2$  orthorhombic phases under ambient conditions (Figure 4) [37]. Due to the similarities between lattice parameters, a structural model based on  $Pbca$  was applied to the data collected in the pressure range 24.5–43.3 GPa, and these refinements yield good fits to the experimental profile,  $R_{\text{Bragg}} = 8.1\%$ . From the variation of molar volume ( $V/Z$ ) of  $PbO_2$  phases with pressure, it is clear that two structural transitions occur, around  $\sim 24$  GPa and  $\sim 43$  GPa, accompanied by unit-cell volume changes of  $\sim 7.8\%$  and  $\sim 6.7\%$  (Figure 5). We do not find the baddeleyite-type structure in room temperature compression measurements, as reported by Grocholski et al [4]. The phase-transition sequence with increasing pressure is mixed phase ( $\alpha\text{-PbO}_2 + \beta\text{-PbO}_2$ )  $\rightarrow Pbca \rightarrow$  cotunnite phase. Our work thus finds the pure stable cotunnite phase without laser heating, in contrast with the results of Grocholski et al [4] and Haines et al. [19] who observed the cotunnite

phase mixed with *PbCa* between 29 to 47 GPa. As discussed below, the apparent disparities in observations can be attributed to differences in shear stresses present in each experiment.

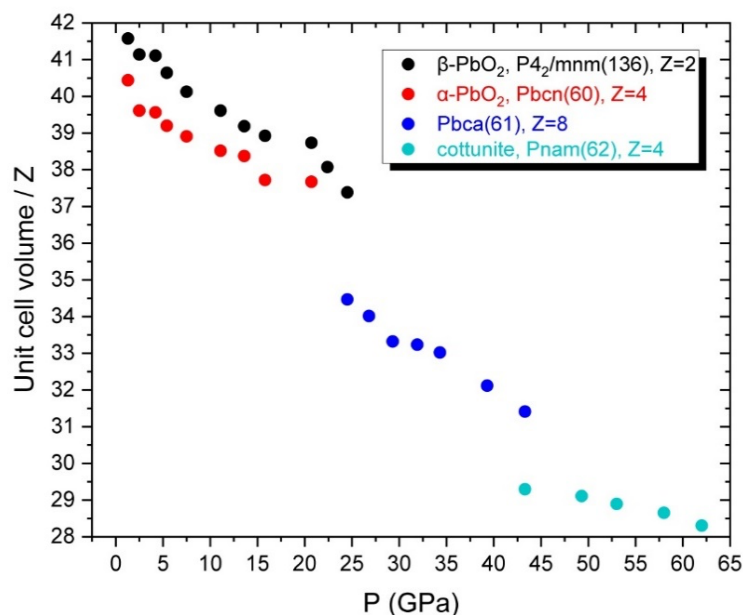


**Figure 5.** Measured unit-cell volumes for  $\beta$ -PbO<sub>2</sub> ( $Z = 2$ ),  $\alpha$ -PbO<sub>2</sub> ( $Z = 4$ ), orthorhombic *Pbca* ( $Z = 8$ ) and *Pnam* ( $Z = 4$ ) phases on compression at room temperature. Uncertainties are smaller than the symbol sizes. Solid lines are least squares fits.

### *b. Melt-PbO<sub>2</sub> under pressure*

The structural evolution of liquid PbO<sub>2</sub> was studied using high pressure-high temperature in-situ diffraction. Melt phases were obtained at 901 K and 4 GPa, and at 773 K and 8 GPa indicating a crystal-liquid phase boundary with a negative P-T slope,  $dP/dT = -0.031 \text{ GPaK}^{-1}$ . Since the entropy upon melting is positive, the negative slope implies that liquid PbO<sub>2</sub> is denser than the parent crystal PbO<sub>2</sub>. [Figure 6a](#) shows our experimental structure-factor ( $S(Q)$ ) patterns and corresponding EPSR simulations, with partial structure factors (PSF) for Pb–Pb, Pb–O and O–O pairs, obtained from these simulations, shown in [Figure 6b-d](#). Reduction of the raw scattering data to structure factors, and derivation of PSFs by direct inversion of the total  $S(Q)$  are described

in Ref. 38 and 39. Simulated partial structure factors indicate that the most dominant contribution to the principal peak located at  $2.1 \text{ \AA}^{-1}$  in the  $S(Q)$  comes from Pb–Pb (dominant) and O–O correlations; Pb–O anti-correlations cause a partial cancellation of the principal peak. The principal peak of  $S(Q)$  at 773 K and 8 GPa is more intense than that at 901 K and 4 GPa, suggesting more ~~extended~~ short range structural order at a length scale of  $\sim 2.9 \text{ \AA}$  manifested by Pb–Pb and O–O correlations. The most prominent peak in the O–O partial structure factor for the 4 GPa data has a clear shoulder on the low- $Q$  side, which is distinct from the results at 8 GPa that show a broad peak in the  $Q = 1.8\text{--}3.4 \text{ \AA}^{-1}$  range attributable to overlapping of the prominent peak and shoulder.

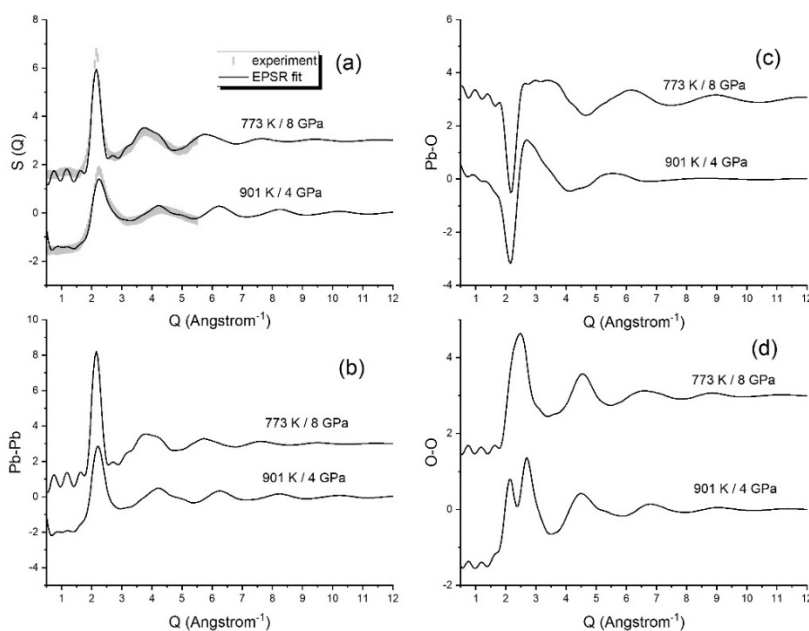


**Figure 6.** (a) Total structure factors,  $S(Q)$  at 901 K and 4 GPa (*bottom curves*), and at 773 K and 8 GPa (*top curves*). Partial structure factors for Pb–Pb (b), Pb–O (c), and O–O (d) pairs calculated from EPSR simulations.

Structural analysis in real space was conducted using the experimental and simulated radial distribution functions (RDF), as summarized in Figure 7. It is clear that the RDFs at the two pressure-temperature conditions (Figure 7a) are not significantly different from each other in terms

of their shapes, except for the peak positions. The corresponding Pb-Pb, Pb-O and O-O pair distribution functions (Figure 7b-d) determined from EPSR simulations indicate that all nearest-neighbor correlations contribute to the first peak in the RDFs. The Pb-Pb, Pb-O and O-O nearest-neighbor distances are calculated to be in the range of 3.2-3.5 Å, 2.2-2.5 Å and 2.9-3.1 Å, respectively. The broadening observed for the first Pb-O peak at 4 GPa data can be attributed to a range of coordination numbers being present around Pb. Nearest-neighbor O-coordination numbers around Pb-atoms,  $n_{PbO}$ , obtained by integrating the area of the corresponding peak in the Pb-O PDF are 7.8(7) and 8.7(6) for 4 GPa and 8GPa, respectively. This trend shows that with rising pressure, the coordination number of oxygen around lead in the melt gradually increases to  $n_{PbO} \approx 9-10$ . This reflects the 4- to 5- coordination of Pb around O with rising pressure, consistent with the calculated  $n_{OPb}$  values that increase from 3.8(4) at 4 GPa to 4.3(4) at 8 GPa.

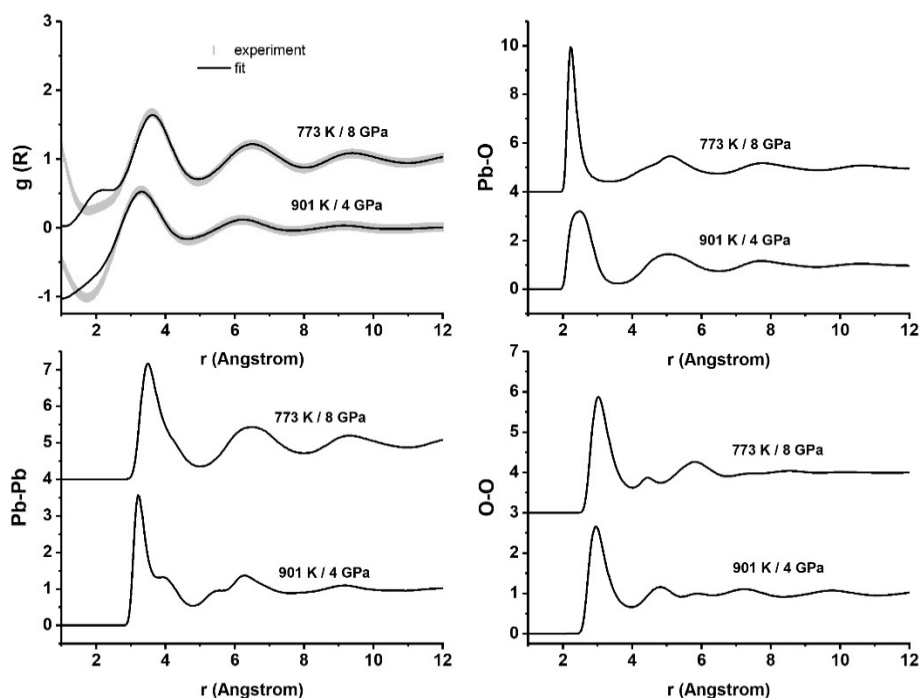


Figure 7. Experimental and simulated radial distribution functions (RDF) at 901K/4GPa (bottom curves) and 773K/8GPa (top curves), and corresponding Pb-Pb, Pb-O and O-O pair distribution functions calculated from the EPSR simulations

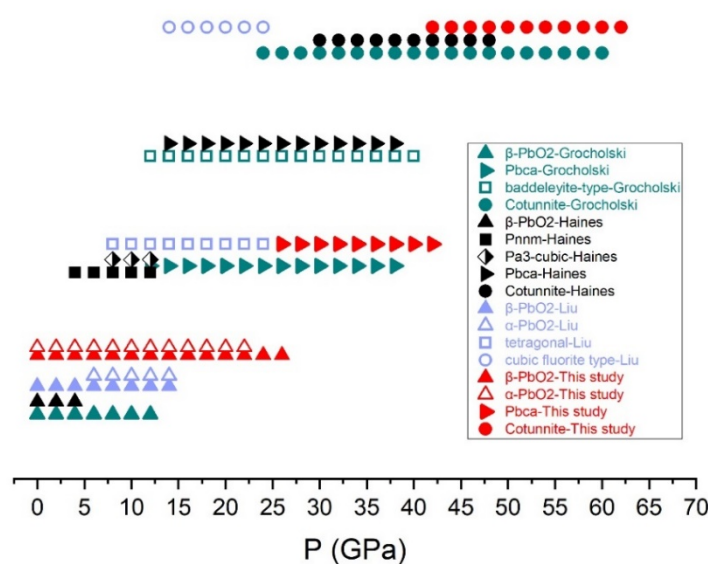
*c. Discussion*

Figure 8 summarizes our results in comparison with the phase transitions reported for  $\text{PbO}_2$  by Liu [40], Haines et al. [36] and Grocholski et al. [4]. A comparison of the onset pressures for the phase transitions from the starting phase to orthorhombic ( $Pbca$ ), and for the formation of the high-pressure cotunnite-type structure indicates that all transitions start at significantly higher pressures in our case as compared to those reported by Haines et al. [36] and Grocholski et al. [4]. These differences lead us to conclude that the pressure transmitting medium ~~could be~~ is a key factor affecting the pressure-induced transformations of  $\text{PbO}_2$ , with shear stresses (i.e., non-hydrostatic conditions) and resulting defects helping to overcome kinetic barriers to transformation.

Specifically, we used Ne whereas Haines et al. [36] and Grocholski [4] used silicone grease and Ar as pressure media, respectively, which provide less hydrostatic conditions as compared with Ne. The difference between Ne and Ar is related to the difference in their atomic radii, Ne (0.38 Å) and Ar (0.71 Å), and consequently, Ar shows a low solidification pressure, ~1.4 GPa at room temperature (4.8 GPa for Ne), and a hydrostatic limit of ~9 GPa (~15 GPa for Ne). Silicon grease supports even larger deviatoric stresses, as compared to noble gases, and therefore causes the appearance of phase transitions at lower pressures.

Moreover, Haines and Grocholski report that the cotunnite-type structure ( $Pnam$ ) was found coexisting with the orthorhombic ( $Pbca$ ) and baddeleyite structures in the pressure ranges ~22 to 40 GPa [4] and ~30 to 40 GPa [36]. Liu reported the cubic fluorite-type structure as the high-pressure phase in the range of 12-22 GPa, coexisting with the tetragonal form [40]. Our results do not show any phase coexistence above ~25 GPa, and this ~~may be~~ is attributed to the

largely hydrostatic conditions of the present study, i.e., the absence of significant shear stress or strain in the sample chamber, making the  $(\beta\text{-PbO}_2 + \alpha\text{-PbO}_2) \rightarrow \text{Pbca} \rightarrow \text{cotunnite-type}$  structure transition pathway favorable in our study. It should also be noted that the pressure-induced phase transition sequence of  $\text{PbO}_2$  seems to be sensitive to the starting phase, which was a mixture of rutile structured  $\beta\text{-PbO}_2$  (dominant) and orthorhombic  $\alpha\text{-PbO}_2$  (minor) in our case whereas Liu [40], Haines et al. [36] and Grocholski et al. [4] started with exclusively rutile structured  $\beta\text{-PbO}_2$ .



**Figure 8.** Summary of compression results obtained in the present study, alongside the phase transitions reported for  $\text{PbO}_2$  by Liu [41], Haines et al. [37] and Grocholski [4].

The cotunnite structure consisting of nine-fold coordinated cations is the expected structure of silica in the multi-Mbar regime. Therefore, this leads us to consider melt- $\text{PbO}_2$  as an important analog for liquid metallic silicates at the extreme conditions relevant to the interiors of large planets. Our results obtained from molten  $\text{PbO}_2$  provide evidence for highly coordinated Pb-cations, with the first-neighbor coordination of O around Pb increasing from about 7.8(7) to 8.7(6) between 4-8 GPa.

#### IV. CONCLUSIONS

Up to 65 GPa,  $\text{PbO}_2$  is found to undergo two transitions at room temperature, beginning with a mixture of rutile and orthorhombic structures and ending with the cotunnite structure. The first transition is to a  $Pbca$  phase, observed at  $\sim 22$  GPa, with a further transition to the cotunnite phase at  $\sim 43$  GPa corresponding to a change in coordination number around Pb-atoms from 6 to 7 and to 9, respectively. We find the pure cotunnite phase without laser heating. The  $\text{ZrO}_2$ -type  $Pbca$  phase transforms to  $\alpha\text{-PbO}_2$  ( $Pbcn$ ) scrutinyite phase upon decompression below 13 GPa, and this is retained down close to ambient pressure. Compared to previous studies reported by Haines et al. [36] and Grocholski et al. [4], all transitions observed in our study start at significantly higher pressures, indicating that the pressure transmitting medium influences the transformation kinetics and perhaps the phase stability via the amount of deviatoric stress and strain that are present. The distribution of coordination numbers in melt- $\text{PbO}_2$ , obtained by empirical potential structure refinements of x-ray diffraction patterns, suggest the range of liquid metallic silicates structures achieved at extreme planetary conditions.

#### ACKNOWLEDGMENTS

The Advanced Light Source is supported by the Director, Office of Science, Office of Basic Energy Sciences, of the U.S. Department of Energy under Contract No. DE-AC02-05CH11231, and by COMPRES, the Consortium for Materials Properties Research in Earth Sciences under NSF Cooperative Agreement EAR 10-43050. BKG acknowledges help provided by T. J. Smart in the procurement of the sample and initial help with the experiment. We also thank support from the NNSA through CMEC at UCSD and from NSF through CMAP at University of Rochester.

## References

1. M. Millot, N. Dubrovinskaia, A. Cernok, S. Blaha, L. Dubrovinsky, D. G. Braun, P. M. Celliers, G. W. Collins, J. H. Eggert, R. Jeanloz, Shock compression of stishovite and melting of silica at planetary interior conditions, [Science 347, 418-420 \(2015\)](#).
2. V. P. Prakapenka, G. Shen, L. S. Dubrovinsky, M. L. Rivers, S. R. Sutton, High pressure induced phase transformation of SiO<sub>2</sub> and GeO<sub>2</sub>: difference and similarity, [J. Phys. & Chem. Solids 65, 1537-1545 \(2004\)](#).
3. Y. Kuwayama, K. Hirose, N. Sata, Y. Ohishi, The pyrite-type high pressure form of silica, [Science 309, 923-925 \(2005\)](#).
4. B. Grocholski, S-H. Shim, E. Cottrell, V. B. Prakapenka, Crystal structure and compressibility of lead oxide upto 140 GPa, [American Mineralogist 99, 170-177 \(2014\)](#).
5. A. R. Oganov, M. J. Gillan and G. D. Price, Structural stability of silica at high pressures and temperatures, [Phys. Rev. B 71, 064104-064108 \(2005\)](#).
6. K. Umemoto, R. Wentzcovitch, P.B. Allen, Dissociation of MgSiO<sub>3</sub> in cores of gas giants and terrestrial exoplanets, [Science 311, 983-986 \(2006\)](#).
7. T. Tsuchiya, J. Tsuchiya, Prediction of a hexagonal SiO<sub>2</sub> phase affecting stabilities of MgSiO<sub>3</sub> and CaSiO<sub>3</sub> at multimegabar pressures, [Proc. Natl. Acad. Sci. USA 108, 1252-1255 \(2011\)](#).
8. S. Wu, K. Umemoto, M. Ji, C-Z. Wang, K-M. Ho, R. M. Wentzcovitch, Identification of post-pyrite phase transitions in SiO<sub>2</sub> by a genetic algorithm, [Phys. Rev. B 83, 184102-4 \(2011\)](#).
9. Y. Usui, and T. Tsuchiya, Ab initio two phase molecular dynamics on the melting curve of SiO<sub>2</sub>, [J. Earth Sci. 21, 801-810 \(2010\)](#).
10. M. J. Lyle, C.J. Pickard, R. J. Needs, Prediction of 10-fold coordinated TiO<sub>2</sub> and SiO<sub>2</sub> structures at multi-megabar pressures, [Proc. Natl. Acad. Sci. USA 112, 6898-6901 \(2015\)](#).
11. Y. Al-Khatatbeh, B. Kiefer, and K. M. Lee, High -pressure behavior of TiO<sub>2</sub> as determined by experiment and theory, [Phys. Rev. B 79, 134114-8 \(2009\)](#).
12. N.A. Dubrovinskaia, L. Dubrovinsky, R. Ahuja, V. B. Prokopenko, V. Dmitriev, H.-P. Weber, J. M. Osorio-Guillen, B. Johansson, Experimental and theoretical identification of a new high-pressure TiO<sub>2</sub> polymorph, [Phys. Rev. Lett. 87, 275501-4 \(2001\)](#).

13. H. Dekura, T. Tsuchiya, Y. Kuwayama, J. Tsuchiya, Theoretical and experimental evidence for a new post-cotunnite phase of titanium dioxide with significant optical absorption, [Phys. Rev. Lett. \*\*107\*\*, 045701-4 \(2011\)](#).
14. X. Zhong, J. Wang, S. Zhnag, G. Yang, and Y. Wang, Ten-fold coordinated polymorph and metallization of TiO<sub>2</sub> under high pressure, [RSC Adv. \*\*5\*\*, 54253-54257 \(2015\)](#).
15. J. P. Itie, A. Polian, and J. M. Besson, Optical-absorption edge of CsI up to 58 GPa, [Phys. Rev. B \*\*30\*\*, 2309-2311 \(1984\)](#).
16. J. Haines, J. M. Leger, and C. Chateau, Transition to a crystalline high pressure phase in  $\alpha$ -GeO<sub>2</sub> at room temperature, [Phys. Rev. B \*\*61\*\*, 8701-8706 \(2000\)](#).
17. S. Ono, T. Tsuchiya, K. Hirose, and Y. Ohishi, High-pressure form of pyrite-type germanium dioxide, [Phys. Rev. B \*\*68\*\*, 014103-014103-5 \(2003\)](#).
18. Z. Lodziana, K. Parlinski, and J. Hafner, Ab initio studies of high-pressure transformations in GeO<sub>2</sub>, [Phys. Rev. B \*\*63\*\*, 134106-7 \(2001\)](#).
19. J. Haines, and J. M. Leger, X-ray diffraction study of the phase transitions and structural evolution of tin di oxide at high pressure: Relationships between structure types and implications for other rutile-type dioxides, [Phys. Rev. B \*\*55\*\*, 11144-11154 \(1997\)](#).
20. S. Ono, K. Funakoshi, A. Nozawa, and T. Kikegawa, High- pressure phase transitions in SnO<sub>2</sub>, [J. Appl. Phys. \*\*97\*\*, 073523-1-5 \(2005\)](#).
21. S. R. Shieh, A. Kubo, T. S. Duffy, High pressure phases in SnO<sub>2</sub> to 117 Gpa, [Phys. Rev. B \*\*73\*\*, 014105-1-014105-7 \(2006\)](#).
22. E. A. Petigura, A. W. Howard, G. W. Marcy, Prevalence of Earth-size planets orbiting sun like stars, [Proc. Natl. Acad. Sci. USA \*\*110\*\*, 19273-19278 \(2013\)](#).
23. S. Mazevet, T. Tsuchiya, A. Benuzzi-Mounaix, F. Guyot, Melting and metallization of silica in the cores of gas giants, ice giants, and super Earths, [Phys. Rev. B \*\*92\*\*, 014105-4 \(2015\)](#).
24. H. K. Mao, J. Xu, P. M. Bell, Calibration of the ruby pressure gauge to 800kbar under quasi-hydrostatic conditions, [J. Geophys. Res. \*\*B91\*\*, 4673-4676 \(1986\)](#).
25. S. V. Raju, J. M. Zaug, B. Chen, J. Yan, J. Knight, R. Jeanloz, and S. M. Clark, Determination of the variation of the fluorescence line positions of the ruby, strontium tetraborate, alexandrite and strontium-doped ytterium aluminum garnet with pressure and temperature, [J. Appl. Phys. \*\*110\*\*, 023521-1-023521-8 \(2011\)](#).
26. M. Kunz, A. A. MacDowell, A. W. Caldwell, D. Cambie, R. S. Celestre, E. E. Domning, R. M. Duarte, A. E. Gleason, J. M. Glossinger, N. Kelez, D. W. Plate, T. Yu, J. M. Zaug, H. Padmore, R. Jeanloz, P. Alivisatos, and S. M. Clark, A beamline for high pressure studies at the

- Advanced Light Source with a superconducting bending magnet as the source, [Journal of Synchrotron Radiat.](#) **12**, 650-658 (2005).
27. A. P. Hammersley, FIT2D: A Multipurpose Data Reduction, analysis and visualization program, [J. Appl. Cryst.](#) **49**, 646-652 (2016).
  28. C. Prescher, V. B. Prakapenka, DIOPTAS: a program for reduction of two dimensional X-ray diffraction data and data exploration, [High Press. Res.](#) **35**, 223-230 (2015).
  29. Basic demonstration of Celref unit cell refinement software on a multiphase system  
The CCP14 Home page at <http://www.ccp14.ac.uk>.
  30. A. C. Larson, and Von Dreele, Rietveld Refinement Program, GSAS, Laboratory Report LAUR 86-748 (2004).
  31. A. K. Soper, On the uniqueness of structure extracted from diffraction experiments on liquids and glasses, [J. Phys.: Condens. Matter](#) **19**, 415108 (2007).
  32. A. K. Soper, Empirical potential Monte Carlo simulations of fluid structure, [Chem. Phys.](#) **202**, 295-306 (1996).
  33. O. L. G. Alderman, A. C. Hannon, D. Holland, S. Feller, G. Lehr, A. J. Vitale, U. Hoppe, M. v Zimmermann, A. Watenphul, Lone-pair distribution and plumbite network formation in high lead silicate glass, 80PbO·20SiO<sub>2</sub>, [Phys. Chem. Chem. Phys.](#) **15**, 8506-8519 (2013).
  34. C. Y. Maghfiroh *et al* 2020, Parameters ( $\sigma$ ,  $\epsilon$ ) of Lennard-Jones for Fe, Ni, Pb for Potential and Cr based on Melting Point Values Using the Molecular Dynamics Method of the Lammmps Program, [J. Phys.: Conf. Ser.](#) **1491**, 012022 (2020).
  35. W. B. White, F. Dache, and R. Roy, High-Pressure-High-Temperature Polymorphism of the Oxides of Lead, [Journal of the American Ceramic Society](#) **44**(4), 170 -174 (1961).
  36. J. Haines, J. M. Leger, and O. Schulte, The high pressure phase transition sequence from the rutile-type through to the cotunnite-type structure in PbO<sub>2</sub>, [J. Phys.: Condens. Matter](#) **8**, 1631-1646 (1996).
  37. O. Ohtaka, T. Yamanaka, S. Kume, N. Hara, H. Asano and F. Izumi, Structural Analysis of Orthorhombic ZrO<sub>2</sub> by High Resolution Neutron Powder Diffraction, [Proc. Japan Acad. B](#) **66**, 193-196 (1990).
  38. B. Kalkan, B. Godwal, S.V. Raju, *et al.*, Local structure of molten AuGa<sub>2</sub> under pressure: Evidence for coordination change and planetary implications, [Sci. Rep.](#) **8**, 6844 (2018).
  39. A. K. Soper, Partial structure factors from disordered materials diffraction data: An approach using empirical potential structure refinement, [Phys. Rev. B](#) **72**, 104204/1–104204/12 (2005).
  40. Lin-gun Liu, The High-Pressure Phase Transformations of PbO<sub>2</sub>: An in-situ X-ray Diffraction Study, [Phys. Chem. Minerals](#) **6**, 187-196 (1980).